RESEARCH PAPER

Monte Carlo simulation of Au@MNP nanoparticles for MRI-guided proton therapy: tailoring core-shell architecture for dose enhancement

Maryam Bordbar[1], Mohammadreza Parishan[1*], Rasool Safari[1], Zahra Rakeb[1]

[1]Department of Nuclear Engineering, School of Mechanical Engineering, Shiraz University, Shiraz, Iran

ABSTRACT

Objective(s): Integrating magnetic resonance imaging (MRI) with proton therapy holds significant promise for enhancing treatment efficacy. Magnetic nanoparticles (MNPs), such as gadolinium and superparamagnetic iron oxide nanoparticles (SPIONs), are well-known for improving tissue contrast in MRI. In this study, we investigate the potential of core–shell nanoparticles (Au@MNPs) as agents that can enhance the delivery of therapeutic doses to targeted tissues. Specifically, we examine how variations in core diameter and shell thickness, using either gadolinium oxide (Gd_2O_3) or SPION shells, influence dose enhancement.

Materials and Methods: A simulated proton beam with a weighted energy spectrum—representing both primary and secondary protons within the Spread-Out Bragg Peak (SOBP) region—was used to irradiate the nanoparticles. The energy deposited within the nanoparticles, as well as the phase space of surrounding secondary particles, was evaluated. Key parameters, including energy efficiency, total energy release, and the number of secondary electrons, were analyzed to compare the performance of various nanoparticle designs.

Results: Our findings indicate that incorporating a gold core is advantageous for thin magnetic layers (<15 nm), as it enhances the dose around the nanoparticle while maintaining a size compatible with MRI applications (<20 nm). In contrast, for thicker magnetic layers (greater than 20 nm), a larger gold core diameter is required to achieve effective dose enhancement.

Conclusion: These results suggest that embedding a gold core with a diameter of less than 15 nm within MRI-compatible nanoparticles is a promising strategy for enhancing dose delivery in proton therapy. Further studies are warranted to investigate the impact of core–shell nanoparticles on magnetic properties, which are critical for their theranostic potential.

Keywords*: Theranostic nanomedicine, Radiosensitizing agents, Proton therapy, Magnetic Resonance imaging, Metal nanoparticles, Monte Carlo method.*

How to cite this article

Bordbar M, Parishan M, Safari R, Rakeb Z. Monte Carlo simulation of Au@MNP nanoparticles for MRI-guided proton therapy: tailoring core-shell architecture for dose enhancement. Nanomed J. 2026; 13(2): 344-355. *DOI: 10.22038/NMJ.2025.81909.2039*

INTRODUCTION

MRI-guided proton therapy represents a significant advancement in cancer treatment by synergistically combining the characteristic Bragg peak profile of proton beams with the real-time imaging capabilities of magnetic resonance imaging (MRI) [1,2]. This integration enables highly conformal dose delivery to tumor targets while minimizing exposure to surrounding healthy tissues, thereby supporting a more personalized and potentially curative treatment approach [3]. Nanoparticles—particularly superparamagnetic iron oxide nanoparticles (SPIONs) and gadolinium (Gd)-based nanoparticles—exhibit high biocompatibility and tunable surface properties [4]. These characteristics, along with their intrinsic magnetic properties, make them promising candidates not only as T1 and T2 MRI contrast agents but also for magnetic hyperthermia and various other medical applications [5–8].

The fight against cancer has also highlighted a critical role for metallic nanoparticles (NPs) in radiation therapy [9,10]. By incorporating NPs into radiotherapeutic protocols, researchers aim to enhance treatment efficacy against cancer cells while minimizing—or at least maintaining—the risk of complications in healthy tissues [11]. A wide

* *Corresponding author:* Mohammadreza Parishan, Ph.D. Department of Nuclear Engineering, School of Mechanical Engineering, Shiraz University, Shiraz, Iran. Tel: +98 71 36473474, Emails: *m.r.parishan@shirazu.ac.ir*.

Note. This manuscript was submitted on August 13, 2024; approved on July 01, 2025.

range of elements, from titanium (atomic number 22) to bismuth (atomic number 83), is currently being investigated as potential dose-enhancing agents in conventional photon-based radiotherapy and ion therapy [12,13]. Although both SPIONs and gadolinium-based magnetic nanoparticles (MNPs) have been studied for their dose-enhancing potential [14–17], gold nanoparticles (AuNPs) have attracted significantly greater research interest due to their advantageous combination of high atomic number, high density, and excellent biocompatibility [18–21]. Proton irradiation of NPs can result in localized dose enhancement through the generation of low-energy secondary electrons. It is hypothesized that a substantial fraction of these excess electrons, observed in the secondary electron spectra emitted from the NPs, originates from Auger electron emission processes [22,23].

SPIONs and gadolinium-based nanoparticles can be simultaneously utilized for both imaging and dose enhancement. Incorporating gold into these nanoparticles further amplifies their dose-enhancing capabilities. The integration of magnetic nanoparticles with gold can take various structural forms, one of which is the Au@MNP configuration, where gold serves as the core and the magnetic material forms the outer shell [24]. This theranostic nanoparticle structure has been investigated for a wide range of medical applications [25,26]. One advantage of this hybrid design is that it largely preserves the magnetic properties of the nanoparticle, thereby maintaining its efficacy as an MRI contrast agent [27]. Additionally, secondary electrons generated in the gold core experience less attenuation as they traverse the magnetic shell, and electrons produced within the shell can also directly contribute to dose enhancement.

A limited number of studies have investigated the radiosensitizing properties of core–shell nanoparticles, particularly in the context of radiation therapy. To the best of our knowledge, only two studies have specifically examined core–shell structures for this purpose. Slama et al. explored the potential of 8 nm Fe_3O_4@Au core–shell nanoparticles to enhance radiation-induced effects on redox status, pro-inflammatory markers, and cell death in A549 human lung cancer cells [28]. In their study, megavoltage (MV) X-rays were applied at a dose rate of 600 cGy/min, and the results demonstrated that Fe_3O_4@Au nanoparticles significantly increased the radiosensitivity of cancer cells. In another study, Xu et al. employed Monte Carlo simulations to evaluate the physical dose enhancement of Fe_3O_4@Au core–shell nanoparticles (comprising a 60 nm Fe_3O_4 core and a 20 nm Au shell) under irradiation with a 50 keV photon beam [29]. Both studies confirmed the potential of Fe_3O_4@Au nanoparticles as effective radiosensitizers. However, these investigations were limited to X-ray irradiation, and date, no research has addressed the radiosensitization effects of core–shell nanoparticles in the context of proton therapy. This gap underscores the novelty of our current study, which aims to explore the potential of core–shell nanoparticles for dose enhancement in proton therapy.

Several methods have been successfully developed for the synthesis of Au@MNP core–shell nanostructures. For example, Orlando et al. synthesized gold–maghemite (Au@γ-Fe_2O_3) core–shell nanoparticles by nucleating an iron oxide shell onto pre-synthesized gold seeds, resulting in particles approximately 16 nm in diameter with a 4.7 nm outer shell [30]. Similarly, Lin and Doong fabricated Au@Fe_3O_4 yolk–shell nanocatalysts via thermal decomposition of iron pentacarbonyl, yielding nanoparticles with diameters ranging from 8 to 15 nm and shell thicknesses of 2.0–2.4 nm [31]. Another approach, reported by Shevchenko et al., involved the random nucleation of iron onto pre-formed gold nanoparticles through thermal decomposition, producing Au@SPIONs with core diameters of 4. 5 nm and shell thicknesses of 2.5–3.3 nm [32].

Furthermore, Liu et al. prepared bifunctional Au@Fe_3O_4 hybrid core–shell nanoparticles by first synthesizing Au nanoparticles via thermal reduction, followed by the thermal decomposition of $Fe(acac)_3$ on the gold surface [33]. The resulting particles exhibited an average diameter of 11 nm, comprising an 8 nm gold core. Umut et al. synthesized Au@Fe_3O_4 hybrid nanoparticles as potential MRI contrast agents using wet chemical methods, producing particles with gold cores ranging from 5 to 8 nm and an average overall diameter of 15.9 nm [34]. Additionally, Oliveira-Filho et al. synthesized Au@Fe_3O_4 core–shell nanoparticles via thermal decomposition, yielding nanocomposites with a 10.5 nm gold core and a 1.85 nm thick shell [35]. Felix et al. also investigated Au@Fe_3O_4 core–shell nanoparticles fabricated through thermal decomposition, resulting in particles with a 6.9 nm gold core and a 3.5 nm Fe_3O_4 shell [36].

Collectively, these studies highlight the versatility of core–shell nanoparticle synthesis methods and demonstrate the potential for precise control over core and shell dimensions to meet the specific requirements of various biomedical applications.

The impact of core size and magnetic shell thickness on the dose enhancement efficacy of Au@MNP nanoparticles during proton radiotherapy was investigated using Monte Carlo simulations. This study examines the interplay between the increased probability of proton interactions and the self-absorption of secondary electrons within the nanoparticle structure. While enlarging the core and shell can improve the likelihood of proton collisions, it may also intensify intra-nanoparticle absorption of therapeutic secondary electrons. Moreover, given the limited tissue uptake of nanoparticles, their mass concentration must be carefully optimized to achieve the desired effect. Therefore, achieving a balance among core size, shell thickness, and total nanoparticle mass is essential for maximizing dose deposition. In this work, we evaluate the dosimetric performance of Au@MNP nanoparticles with varying geometrical configurations under proton irradiation using Monte Carlo methods. Due to the inherent complexities involved, the magnetic properties of these nanoparticles will be addressed in future studies focused on synthesis and characterization.

The subsequent sections outline the methodology used to simulate a proton beam with a weighted energy spectrum that reflects interactions with nanoparticles at various depths within the tumor. This approach accounts for spatial variations in nanoparticle distribution within the tumor microenvironment. Nanoparticles with varying core sizes and shell thicknesses are irradiated using this beam model, enabling the extraction of key physical and dosimetric parameters. The investigation further examines how nanoparticle mass and energy efficiency impact the formation of secondary particles and the resulting yield of distinct chemical species. We anticipate that these findings will offer valuable guidance in optimizing the design of Au@MNP hybrid theranostic nanoparticles, ultimately supporting effective dose enhancement strategies in proton therapy.

MATERIALS AND METHODS

In pencil beam scanning (PBS) proton therapy, where nanoparticles are uniformly distributed within the tumor volume, individual nanoparticles are exposed to proton beams with varying energy spectra. This variation arises from the stepwise modulation of proton beam energy used to sequentially target different depth layers within the treatment volume. Such spectral heterogeneity necessitates evaluating nanoparticle responses across the full range of incident energies to ensure optimal therapeutic efficacy. An ideal nanoparticle design would either exhibit consistent radiosensitizing performance at the average energy and intensity of the proton beam or be optimized to respond effectively to the weighted energy spectrum characteristic of PBS irradiation

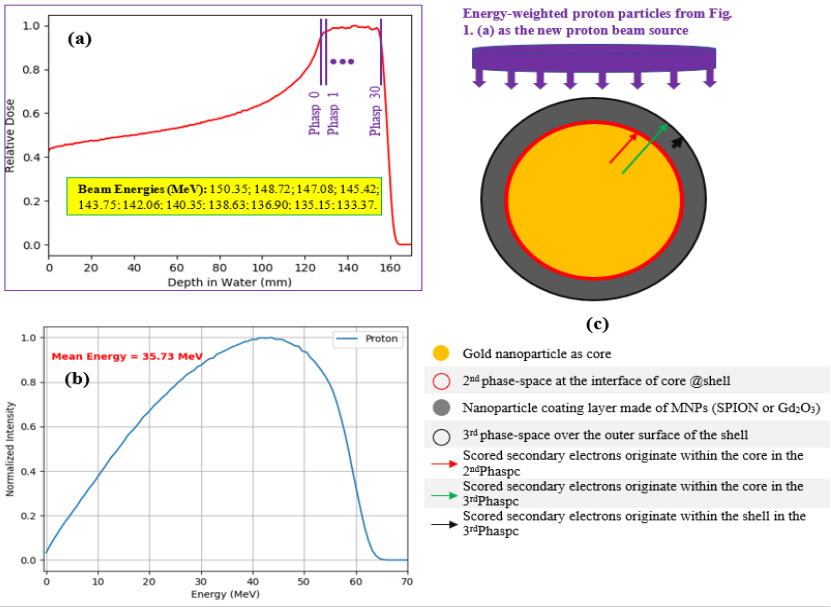

Fig. 1. Simulation geometry and nanoparticle irradiation process. (a): Depth dose profile of proton beams in a water phantom. Thirty-one phase-spaces within the SOBP were recorded at 1.0 mm intervals. (b): Energy spectrum of the proton particles recorded in the 31 phase-spaces in SOBP. (c) A disc-shaped proton source irradiates the nanoparticle. The descriptions of the different part of the nanoparticle are shown at the bottom of the Fig. 1(c).

Monte Carlo simulations were conducted using the TOPAS and TOPAS-nBio toolkits [37–39]. A total of 31 phase spaces, each separated by 1 mm, were extracted from a water phantom irradiated with proton beams (Figure 1a). The proton beam energy and the resulting spread-out Bragg peak (SOBP) are illustrated in Figure 1a. All primary and secondary protons within these phase spaces were incorporated to construct a new proton beam with a weighted energy spectrum, as shown in Figure 1b. Subsequently, a disk-shaped proton source with a diameter equivalent to the nanoparticle size was defined and assigned the weighted energy spectrum (Figure 1b) to simulate nanoparticle irradiation. Protons from this source were emitted in parallel and directed toward the nanoparticle (Figure 1c). For each simulation, approximately 50 million incident protons were used as primary histories.

The nanoparticles investigated in this study consist of a gold core coated with a magnetic component—either superparamagnetic iron oxide (SPION) or gadolinium oxide (Gd_2O_3) nanoparticles—as illustrated in Figure 1c. A comprehensive set of simulations was performed using gold cores with eleven distinct diameters: 3, 5, 7, 9, 12, 15, 20, 30, 40, 50, and 70 nm. The thickness of the magnetic shell was varied across ten values: 0, 5, 7, 10, 15, 20, 25, 30, 40, and 50 nm. Simulations were conducted using the Livermore low-energy physics model, configured with a 10-eV threshold for secondary particle production and a maximum step size of 1 nm. To accurately capture the complete de-excitation cascade, Auger electron emission, fluorescence, and proton-induced X-ray emission (PIXE) were all included. Additionally, the energy cutoff was bypassed during cascading processes to ensure precise modeling of secondary electron emissions.

Following this simulation step, data were collected from three distinct phase spaces: (1) the core–shell interface, capturing secondary particles generated in the core and exiting into the magnetic shell; (2) the outer nanoparticle surface, recording secondary particles originating from both the core and the shell, separated into two distinct datasets. In addition, the total energy deposited by both primary and secondary particles within the entire nanoparticle (core + magnetic shell) was quantified. For subsequent analysis, only electrons were considered, as they are the most abundant and influential contributors to local dose distribution around the nanoparticle.

The collected data were used to generate several visualizations, including the energy spectrum of secondary electrons, their total number, and average energy, analyzed separately for the core and the entire nanoparticle. To evaluate the effect of core size and magnetic shell thickness on dose enhancement efficacy around the nanoparticle, we calculated the ratio of energy emitted from the nanoparticle surface to the total energy transferred to the nanoparticle volume (including both deposited and emitted energy). This ratio, referred to as energy efficiency, serves as a key metric for assessing the nanoparticle's effectiveness in enhancing local dose deposition. For comparison, the energy efficiency of individual SPIONs, Gd_2O_3, gold, and hypothetical water nanoparticles—each with identical mass—was also analyzed. Furthermore, in light of the limited mass concentrations achievable in tumors, the specific energy released per unit nanoparticle mass (mass-normalized energy release) was evaluated.

The complete chemical stage of the simulation was performed for each nanoparticle. The source of secondary particles at the nanoparticle surface was defined using a phase space containing all secondary electrons emitted from the entire nanoparticle volume. Five types of nanoparticles with comparable mass were investigated: gold, SPION, Gd_2O_3, Au@MNP (gold core with magnetic nanoparticle shell), and a hypothetical water nanoparticle surrounded by a 1 mm diameter water sphere. The simulations utilized the TsEmDNAPhysics and TsEmDNAChemistry modules, which account for both physical and chemical interactions. For thermalized solvated electrons, the well-established Ritchie model was used. The diffusion and interaction of chemical species were simulated using the independent reaction times (IRT) method, chosen for its high computational efficiency, which is particularly beneficial for modeling low linear energy transfer (LET) particles, such as electrons. The yields of various chemical species were tracked over time steps ranging from 1 picosecond to 1 microsecond. However, for clarity and brevity, only the results corresponding to two representative species are presented.

RESULTS

Figure 1a illustrates the dose profile and the spread-out Bragg peak (SOBP) generated by proton beams of specific energies within a tumor phantom measuring 3 cm in diameter.

Figure 1b presents the corresponding weighted energy spectrum, derived from 31 phase spaces sampled along the SOBP region. This spectrum has an average energy of 35.73 MeV and displays

negative skewness. The observed skew toward higher energies is attributed to the greater abundance of high-energy protons in phase spaces corresponding to shallower tumor layers—an effect inherent to active pencil beam scanning techniques.

Figure 2 presents the energy spectra of secondary electrons emitted from various nanoparticles with different core diameters and shell thicknesses. All spectra are normalized to the number of primary protons in the beam. Figures 2a and 2b specifically focus on electrons originating from the gold core and reaching the nanoparticle surface. Both spectra exhibit a distinct peak at approximately 1 keV. As shown in Figure 2b, the number of core-originated electrons decreases with increasing shell thickness (either SPION or Gd_2O_3). In contrast, Figure 2a shows that increasing the gold core diameter—while keeping shell thickness constant—leads to a higher number of emitted electrons. In terms of attenuation, the SPION shell exhibits lower attenuation for sub-1 keV electrons compared to the Gd_2O_3 shell. However, this trend reverses at energies above 1 keV, where the Gd_2O_3 shell becomes more transparent to core-emitted electrons.

Figures 2c and 2d depict the energy spectra of secondary electrons emitted from the entire nanoparticle, including both core and shell contributions. At energies below 1 keV, characteristic peaks corresponding to Auger electrons from specific atomic shells of SPION and Gd_2O_3 are evident. Notably, the SPION-coated nanoparticles exhibit a higher intensity of emitted electrons in this low-energy range (below 1 keV). However, this trend reverses at energies above 1 keV, where Gd_2O_3-coated nanoparticles demonstrate greater electron emission.

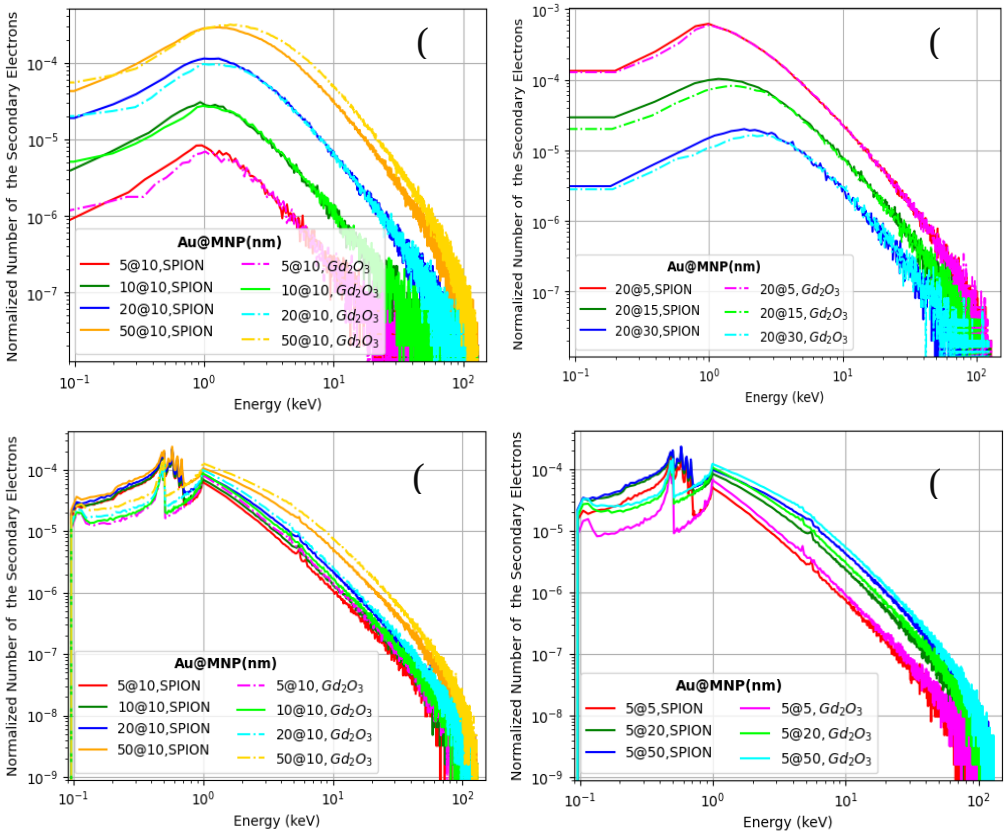

Fig. 2. Energy spectra of secondary electrons reaching the nanoparticle surface following proton irradiation. Variations in core diameter and shell thickness are investigated. The number of energy bins differs between panels (a) and (b) compared to (c) and (d) due to differing analysis requirements. (a) Electrons originating from the nanoparticle core: core diameter is fixed, while MNP shell thickness varies. (b) Electrons originating from the core: core diameter varies, while MNP layer thickness is constant. (c) Electrons originating from the entire NP (core + layer): core diameter is fixed, while MNP layer thickness varies. (d) Electrons originating from the entire nanoparticle: core diameter varies, while MNP layer thickness is constant.

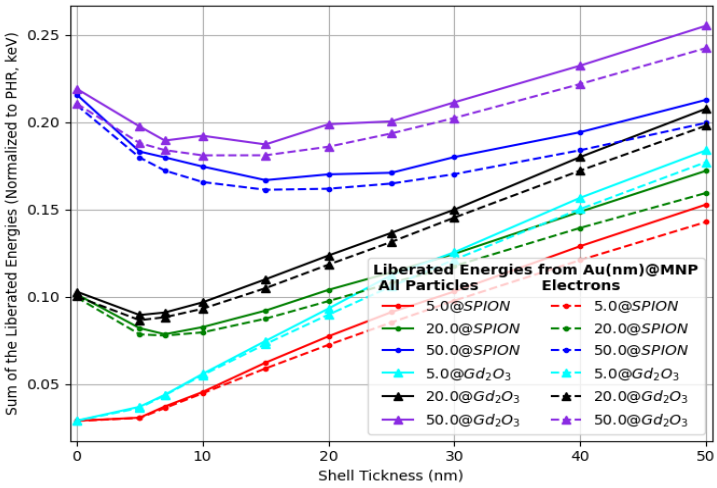

Fig. 3. Total energy released from the outer surface of Au@SPION (circular marker) and Au@Gd_2O_3 (triangular marker) nanoparticles of three different sizes (indicated by legend) following proton irradiation. Continuous lines represent the sum of all secondary particles and photons, while dashed lines depict the contribution solely from secondary electrons.

Figure 3 illustrates the normalized total energy emitted from the nanoparticle surface per incident proton (keV/proton). Two data series are presented: one representing the combined energy emitted by all particles and photons, and the other showing energy emission by secondary electrons only. The figure demonstrates that secondary electrons are the primary contributors to the outward energy flux from the nanoparticle. For a fixed core size, increasing the shell thickness results in a growing divergence between the total emitted energy and the energy attributable solely to secondary electrons. Nevertheless, both curves follow a broadly similar trend. As a result, the remainder of this study will focus exclusively on analyzing secondary electron emission.

Figure 4a illustrates the dependence of emitted electron yield on magnetic shell thickness for various core diameters. For cores smaller than 12 nm, the number of emitted electrons increases with increasing shell thickness. This trend is attributed to two primary factors: (1) the enhanced probability of interactions between the primary proton beam and the nanoparticle due to increased overall interaction volume, and (2) reduced self-absorption of electrons within smaller cores. For cores larger than 12 nm, a different behavior is observed: the number of emitted electrons initially decreases with increasing shell thickness before rising again. The increased likelihood of electron self-absorption within larger cores explains this. In such cases, many of the electrons generated within the core lose energy before reaching the core–shell interface. As a result, even a thin shell may absorb a substantial portion of these low-energy electrons, reducing the overall emitted yield. However, as shell thickness increases further, more electrons generated in the core are fully absorbed within the nanoparticle. Consequently, the emitted electron yield becomes increasingly dominated by electrons produced within the shell. This, combined with rising self-absorption within the thicker shell, leads to a convergence of the emission curves across different core sizes, as observed in Figure 4a.

Figure 4b quantifies the contribution of core-generated electrons to the total emitted yield as a function of shell thickness for various core diameters. The data reveal a rapid decline in this contribution with increasing shell thickness. Notably, the rate of decrease is steeper for smaller cores. For example, a 12 nm gold core shows a sharp drop in its contribution to the total yield, decreasing to approximately 10% when the shell thickness reaches 10 nm. This effect is even more pronounced for a 3 nm core, where the contribution falls to less than 1% at the same shell thickness.

Given the limited tissue uptake of nanoparticles, their mass must be taken into account when evaluating surface-emitted energy. Figure 4c shows the total energy emitted per unit mass of each nanoparticle, normalized by both the number of incident primary protons and the individual nanoparticle mass. The results indicate that, for a fixed core diameter, thinner magnetic shells yield more favorable energy output per unit mass. Furthermore, for a given shell thickness, nanoparticles with smaller cores exhibit higher energy release per unit mass.

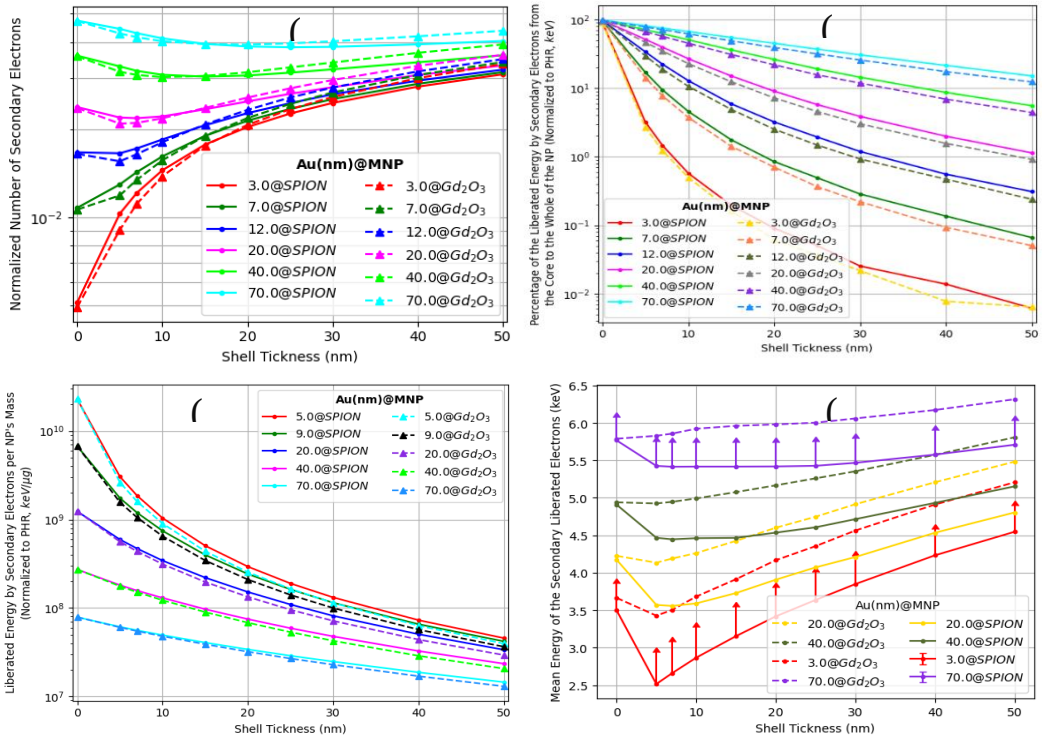

Fig. 4. (a) Number of electrons released from the outer surface of Au@SPION and Au@Gd_2O_3. (b) Percentage contribution of released energy by core electrons to the total energy of all electrons released from the outer surface of the nanoparticle. (c) Normalized released energy by the total secondary electrons to the NP's mass. (d) Mean energy distribution of secondary electrons is depicted. Error bars represent the standard deviation (SD) normalized to the $(5 \times mean\ energy)$ (indicated by circles). Only the positive side of the bars is shown for clarity. For the first three sub*Fig.*s, the parameters are divided to the number of primary protons in the run.

Figure 4d presents the average energy of electrons emitted from the nanoparticle surface. The error bars indicate the relative standard deviation (i.e., the ratio of standard deviation to mean energy) for each data point. For clarity, only one-fifth of the positive error value is displayed. The average electron energy shows a clear dependence on core size. For a fixed shell thickness, the diameter increases with the core diameter. This trend can be attributed to the preferential self-absorption of low-energy electrons within the nanoparticle, which results in a higher mean energy among the electrons that escape. Conversely, for a fixed core size, the average electron energy initially decreases and then increases with increasing shell thickness. This non-monotonic trend is more pronounced for smaller core sizes. The initial decrease is likely due to the increased contribution of Auger electrons generated within the shell, particularly those with energies below 1 keV.

These lower-energy electrons can readily reach the nanoparticle surface, resulting in a decrease in the average energy of the emitted electrons. As the shell thickness increases further, only Auger electrons generated near the outer surface can escape. Simultaneously, higher-energy electrons originating from deeper regions of the shell contribute more significantly, leading to an overall increase in the average energy. This behavior is also reflected in the spectra shown in Figure 1. The observed decrease–increase trend in average energy is more pronounced in nanoparticles containing SPIONs compared to those with Gd_2O_3 shells. This difference can be attributed to the higher abundance of low-energy Auger electrons (below 1 keV) produced in SPIONs. Additionally, for a given core size and shell thickness, Gd_2O_3-coated nanoparticles consistently exhibit higher average emitted electron energies than their SPION-coated counterparts.

Another important metric for evaluating nanoparticle performance is the energy transfer efficiency, defined as the ratio of the energy emitted by the nanoparticle to the total energy absorbed by it. In this study, total absorbed energy includes both the energy deposited within the nanoparticle volume and the energy emitted from its surface. In other words, it represents the total energy lost by incident protons during their interactions with the nanoparticle. Figure 5a presents the energy transfer efficiency as a function of core diameter for various magnetic shell thicknesses.

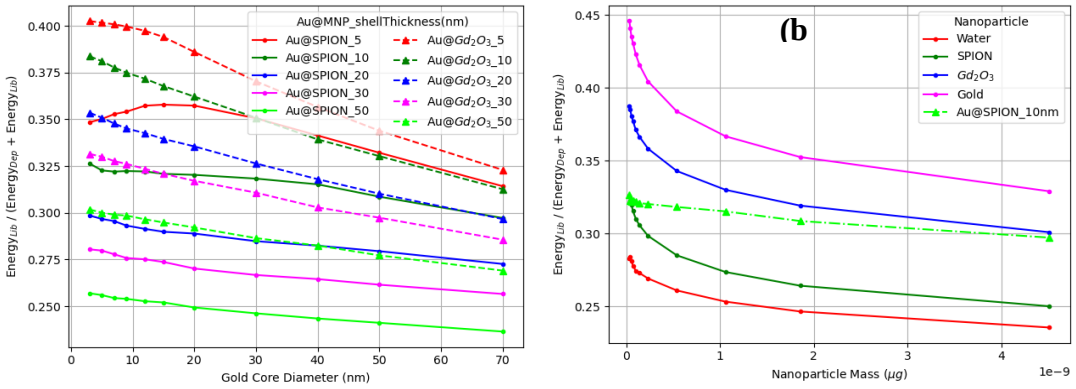

Fig. 5. (a) Energy efficiency, defined as the ratio of deposited energy within the nanoparticle to the total energy released or deposited, is presented for Au@MNP nanoparticles with varying core diameters and MNP shell thicknesses. (b) Energy efficiency defined for single gold nanoparticles, SPION, Gd_2O_3, and a hypothetical water nanoparticle with a mass equivalent to the Au@SPION_10nm configuration. The curve of Au@SPION_10nm nanoparticle are considered for comparison with the curves in Fig.5 (a).

Across all studied nanoparticles, the energy transfer efficiency remains below 40%. However, nanoparticles with Gd_2O_3 shells consistently exhibit higher efficiency compared to those coated with SPIONs. In Gd_2O_3-based nanoparticles, efficiency decreases with increasing gold core diameter, as well as with increasing shell thickness for a fixed core size. A similar trend is observed in SPION-based nanoparticles. However, for SPION shells with a thickness of 5 nm, an initial increase in efficiency is followed by a subsequent decrease as the core diameter increases. This non-monotonic behavior is also expected for SPION shell thicknesses below 5 nm.

Figure 5b compares the energy transfer efficiency of individual nanoparticles—gold (Au), SPION, Gd_2O_3, and hypothetical water—with the trends observed in Figure 5a. In this comparison, an Au@SPION nanoparticle with a 10 nm shell thickness serves as the baseline. By varying the core size of this reference nanoparticle, other single-material nanoparticles with equivalent mass were defined and subjected to proton irradiation. The diagram illustrates energy transfer efficiency as a function of nanoparticle mass. As shown in the figure, nanoparticles composed of elements with higher atomic numbers and physical densities exhibit improved energy transfer efficiency at a fixed mass. Accordingly, the Au@SPION nanoparticle demonstrates higher efficiency than a pure SPION nanoparticle, but remains less efficient than a pure gold nanoparticle. A similar trend is anticipated for Au@Gd_2O_3 structures. Notably, all nanoparticles in Figure 5b show higher efficiency than the hypothetical water nanoparticle, reinforcing the concept of localized dose enhancement through high-Z nanoparticles embedded within tissue.

Figure 6 presents the time-dependent G-values for hydroxyl radicals (•OH) and hydrogen peroxide (H_2O_2) species generated as secondary products from nanoparticle (NP) interactions within a surrounding water medium. The data show that nanoparticles with identical mass produce relatively similar G-values over time, regardless of composition. However, the G-values measured in the vicinity of the hypothetical water nanoparticle are significantly higher than those associated with other nanoparticle types.

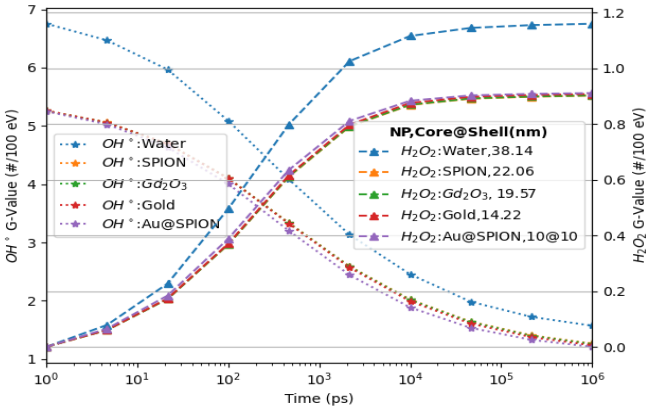

Fig. 6. Comparison of the G-value of two chemical Species for gold, Gd_2O_3, SPION, Au@SPION:10 nm@10 nm, and hypothetical water nanoparticles.

DISCUSSION

This study investigates the design of core–shell nanoparticles (Au@MNP) for dose enhancement in proton therapy, with a dual focus on maximizing energy deposition and preserving the magnetic properties necessary for effective MRI contrast. Monte Carlo simulations were conducted using a weighted energy spectrum that represents the proton beam, including both primary and secondary particles. This spectrum captures variations in beam characteristics experienced by nanoparticles located at different depths within the tumor. Specifically, nanoparticles situated deeper within the tumor are exposed to a proton beam with a distinct energy distribution and particle fluence compared to those closer to the surface. To account for this depth-dependent variation, the weighted spectrum was constructed using phase space data extracted from multiple positions along the tumor depth. Although a 3 cm-diameter tumor located at a 14 cm depth within a water phantom was modeled in this study, it is acknowledged that the energy distribution within the spread-out Bragg peak (SOBP) remains relatively consistent across different depths in water or tissue-equivalent phantoms. For simplicity, this investigation focuses primarily on interactions between the proton beam and the nanoparticles. However, it is recognized that other secondary particles—particularly neutrons and photons generated during therapy—may also contribute to dose enhancement through interactions with nanoparticles in the tumor microenvironment. In particular, neutron interactions with gadolinium-based contrast agents have been shown to further augment local dose deposition [40–42].

An alternative modeling approach could involve simulating nanoparticle interactions exclusively with the specific proton beam encountered at their respective locations within the tumor during each spot scan. This method would effectively place the nanoparticle within the Bragg peak region of individual beamlets, where protons reach their lowest kinetic energy. At these energies, high-Z elements such as gold exhibit near-maximum electronic stopping power, increasing the likelihood of electron interactions and potentially enhancing local dose deposition [43]. However, several additional factors must be taken into consideration. First, the energy of secondary electrons generated during proton–nanoparticle interactions is critical. These electrons must possess sufficient energy to traverse not only the magnetic coating layer but also any biocompatible surface layer surrounding the nanoparticle, to reach the surrounding tissue. Since higher-energy protons produce secondary electrons with greater kinetic energy, they offer improved penetration potential. Second, the number of protons per beamlet decreases progressively with increasing depth in tissue [44]. As a result, nanoparticles located proximal to the beam entrance are exposed to a greater number of protons than those situated near the distal edge or Bragg peak. Finally, even at relatively high nanoparticle concentrations, the probability of a single proton directly interacting with a specific nanoparticle during a single spot scan remains low, due to the small size of individual nanoparticles and the large number of protons delivered per spot area. Therefore, to achieve optimal dose enhancement, it is essential to consider not only the proton energy at the Bragg peak but also the total number of protons delivered across the entire tumor volume, as well as the spatial distribution of nanoparticles during the full course of spot scanning.

The number of electrons generated within hybrid nanoparticles is governed by the interplay between electron production and attenuation processes occurring in both the core and shell regions. When employing gold as the core material and either gadolinium oxide or SPION as the shell, the high density of gold leads to an increased probability of electron production compared to the surrounding shell materials. However, this advantage is offset by the higher likelihood of electron attenuation within gold itself. As a result, for nanoparticles with thin shells, a gold core can be beneficial for enhancing electron yield and, consequently, dose deposition. In contrast, for nanoparticles with thicker shells, the presence of a gold core contributes little to dose enhancement. Instead, it increases the overall nanoparticle mass, a crucial consideration given the clinical limitations on nanoparticle loading. The optimal shell thickness, which is often determined by imaging functionality (e.g., MRI contrast), thus becomes a critical design parameter for balancing radiation dose enhancement with imaging performance and mass constraints.

SPION nanoparticles used for MRI contrast typically range in size from a few nanometers up to approximately 20 nm [45,46]. As shown in Figure 4b, the contribution of core-generated electrons to the total energy emitted from the nanoparticle surface declines sharply with increasing magnetic shell thickness. To ensure nanoparticle sizes remain below the 20 nm threshold for optimal biocompatibility, various combinations of core diameter and shell thickness can be considered. For

example, with a 7 nm gold core and a shell thickness of up to 10 nm, the core electron contribution drops from 100% to approximately 5%. Alternatively, increasing the core diameter to 12 nm while limiting the shell to 8 nm reduces the contribution from 100% to around 20%. These results suggest that incorporating a gold core is beneficial primarily for very small or ultrasmall magnetic nanoparticles. However, in such cases, the potential effect of the gold core on the magnetic properties of the surrounding shell must be carefully evaluated to preserve MRI functionality.

Uncertainties related to chemical reactions at the nanoparticle–water interface, as well as within non-water-based nanoparticles, likely contribute to the observed discrepancies in radiolytic product yields between simulations with water-only and nanoparticle-containing systems. This highlights the need for further investigation. In pure water simulations, the homogeneous environment allows for more straightforward calculation of species production both within the hypothetical water nanoparticle and at its interface. In contrast, for simulations involving other nanoparticles dispersed in aqueous media, the model does not track chemical processes occurring inside the nanoparticles or at their interfaces [47]. This limitation introduces uncertainty into the calculated G-values (radiolytic product yields). Although the simulation accounts for some energy deposition from primary and secondary protons, as well as secondary electrons, within the nanoparticles, this deposited energy is only considered for the hypothetical water nanoparticle and not for others. As a result, the G-values for non-water nanoparticles may be underestimated in comparison. It is essential to acknowledge that the actual G-values for both water and other nanoparticles may differ from the simulated values due to these modeling limitations.

A key limitation of this study is the exclusion of a biocompatible layer over the magnetic shell. While the primary objective was not to quantify absolute dose enhancement, the investigation focused on assessing the influence of core and shell dimensions on secondary electron emission characteristics. Biocompatible coatings—such as polyethylene glycol (PEG)—are known to attenuate both the energy and quantity of electrons reaching surrounding tissues, potentially reducing the dose enhancement effect of nanoparticles [48]. Given the observed similarities in the extracted electron spectra across various nanoparticles, a comparable reduction in secondary electron energy and yield may be expected following the application of a biocompatible layer. However, the specific impact of such a layer is likely to vary depending on its composition, thickness, and density [49]. Further studies are necessary to quantitatively assess the extent of reduction in electron yield and total emitted energy caused by the presence of a biocompatible coating.

Biocompatible coatings are crucial for mitigating the toxicity of superparamagnetic iron oxide and gadolinium oxide nanoparticles when used as MRI contrast agents. Although this study does not quantify the magnetic properties or assess the impact of biocompatible coatings, it is recognized that such layers can significantly alter the energy and yield of emitted secondary electrons, thereby influencing the overall dose enhancement effect. Therefore, while the primary focus of this work is on the relationship between core and shell dimensions and secondary electron emission, the inclusion of biocompatible layers is strongly recommended in future studies, particularly those involving biological systems or in vivo applications.

CONCLUSION

This study investigated the influence of core diameter and magnetic shell thickness on secondary electron emission from Au@MNP nanoparticles containing either Gd_2O_3 or SPION shells. The nanoparticles were irradiated by primary and secondary protons within the Spread-Out Bragg Peak (SOBP) region of a simulated proton beam. Our results indicate that the contribution of core electrons to dose enhancement is inversely proportional to the thickness of the magnetic shell. For small and ultrasmall nanoparticles—typically used as MRI contrast agents—incorporating a gold core can enhance dose delivery while maintaining an overall size compatible with MRI applications (i.e., below 20 nm). In contrast, for thicker magnetic shells, gold cores exceeding 20 nm in diameter may be more effective for dose enhancement; however, such particles may exceed the size limits for MRI and could instead be explored for alternative applications such as magnetic hyperthermia. Overall, our findings suggest that embedding a gold core with a diameter less than 15 nm within MRI-compatible nanoparticles represents a promising approach for enhancing proton therapy dose delivery. Further studies are warranted to assess the impact of these core–shell nanoparticles on magnetic properties, a critical consideration for their theranostic potential.

AUTHOR CONTRIBUTIONS

Maryam Bordbar: Conceptualization, Modeling, Methodology, Writing – Original Draft, Validation, Review & editing. Mohammadreza Parishan: Project Administration, Conceptualization, Modeling, Validation, review. Rasool Safari: Investigation, Writing, review. Zahra rakeb: Methodology, Investigation, review.

ACKNOWLEDGMENTS

This research did not receive any specific grant from funding agencies in the public, commercial, or not-for-profit sectors.

CONFLICT OF INTEREST

The authors declare that they have no conflicts of interest.

REFERENCES

1. Hoffmann A, Oborn B, Moteabbed M, Yan S, Bortfeld T, Knopf A, et al. MR-guided proton therapy: a review and a preview. Radiat Oncol. 2020;15(1):1–13.
2. Gantz S, Karsch L, Pawelke J, Peter J, Schellhammer S, Smeets J, et al. Direct visualization of proton beam irradiation effects in liquids by MRI. Proc Natl Acad Sci U S A. 2023;120(23):e2301160120.
3. Paganelli C, Oborn B, Hoffmann A, Riboldi M. Magnetic resonance imaging in particle therapy. Imaging Part Ther. 2024;7(1):7–21.
4. Smith L, Kuncic Z, Byrne HL, Waddington D. Nanoparticles for MRI-guided radiation therapy: a review. Cancer Nanotechnol. 2022;13(1):1–28.
5. Rahman M. Magnetic resonance imaging and iron-oxide nanoparticles in the era of personalized medicine. Nanotheranostics. 2023;7(4):424–442.
6. Szwed M, Marczak A. Application of nanoparticles for magnetic hyperthermia for cancer treatment—the current state of knowledge. Cancers. 2024;16(6):1156–1172.
7. Papi A, Irajirad R, Yousefvand M, Montazerabadi A, Mohammadi Z. Synthesis and evaluation of SPION@CMD@Ser-LTVSPWY peptide as a targeted probe for detection of HER2+ cancer cells in MRI. Nanomed J. 2021;8(4):279–289.
8. Salehian E, Safa R, Saffari M, Ashrafi S, Farhoudi R, Ebrahimi SES, et al. Synthesis and evaluation of Gd3+-Trp-PLGA as novel nanosized MR tumor imaging candidate. Nanomed J. 2021;8(2):117–123.
9. Peukert D, Kempson I, Douglass M, Bezak E. Metallic nanoparticle radiosensitisation of ion radiotherapy: a review. Phys Med. 2018;52:121–128.
10. Moradi F, Rezaee Ebrahim Saraee K, Abdul Sani SF, Bradley DA. Metallic nanoparticle radiosensitization: the role of Monte Carlo simulations towards progress. Radiat Phys Chem. 2021;180:109294.
11. Tremi I, Spyratou E, Souli M, Efstathopoulos EP, Makropoulou M, Georgakilas AG, et al. Requirements for designing an effective metallic nanoparticle (NP)-boosted radiation therapy (RT). Cancers. 2021;13(13):3185–3201.
12. Schuemann J, Bagley AF, Berbeco R, Bromma K, Butterworth KT, Byrne HL, et al. Roadmap for metal nanoparticles in radiation therapy: current status, translational challenges, and future directions. Phys Med Biol. 2020;65(21):21RM02.
13. Ahmadi Ganjeh Z, Mosleh-Shirazi MA. Macroscopic and microscopic investigation of maximum effectiveness of proton-boron capture therapy using Monte Carlo simulation. Radiat Phys Chem. 2024;214:111289.
14. Díaz-Galindo CA, Garnica-Garza HM. Radiation source personalization for nanoparticle-enhanced radiotherapy using dynamic contrast-enhanced MRI in the treatment planning process. Radiat Phys Chem. 2024;217:111518.
15. Brero F, Calzolari P, Albino M, Antoccia A, Arosio P, Berardinelli F, et al. Proton therapy, magnetic nanoparticles and hyperthermia as combined treatment for pancreatic BxPC3 tumor cells. Nanomaterials. 2023;13(5):791–805.
16. Parishan M, Faghihi R, Kadoya N, Jingu K. The effects of a transverse magnetic field on the dose enhancement of nanoparticles in a proton beam: a Monte Carlo simulation. Phys Med Biol. 2020;65(8):085002.
17. Rafiepour P, Sina S, Mortazavi SMJ, Zabihi A. The effects of magnetic field along with nanoparticles on DNA damage induced by a carbon beam: a Monte Carlo study. 2021 IEEE Nucl Sci Symp Med Imaging Conf Rec NSS/MIC. 2021;1–4.
18. Martinov MP, Fletcher EM, Thomson RM. Multiscale Monte Carlo simulations of gold nanoparticle dose-enhanced radiotherapy II. Cellular dose enhancement within macroscopic tumor models. Med Phys. 2023;50(9):5842–5852.
19. Nath P, Charchi N, Shvydka D, Ray A. Quantitative analysis of reactive oxygen species produced by core-shell gold nanoparticles during radiation therapy. Proc SPIE. 2024;PC12859:PC128590K.
20. Rasouli FS, Masoudi SF. Monte Carlo investigation of the effect of gold nanoparticles' distribution on cellular dose enhancement. Radiat Phys Chem. 2019;158:6–12.
21. Yaftian M, Saeedzadeh E, Khosravi H, Mohammadi E. Evaluation of the effect of gold and iron oxide nanoparticles dispersed on the bolus in radiation therapy by using Monte Carlo simulation. Nanomed J. 2023;10(2):153–162.
22. Wälzlein C, Scifoni E, Krämer M, Durante M. Simulations of dose enhancement for heavy atom nanoparticles irradiated by protons. Phys Med Biol. 2014;59(6):1441–1450.
23. Rudek B, McNamara A, Ramos-Méndez J, Byrne H, Kuncic Z, Schuemann J. Radio-enhancement by gold nanoparticles and their impact on water radiolysis for x-ray, proton and carbon-ion beams. Phys Med Biol. 2019;64(17):175005.
24. León Félix L, Coaquira JAH, Martínez MAR, Goya GF, Mantilla J, Sousa MH, et al. Structural and magnetic

properties of core-shell Au/Fe3O4 nanoparticles. Sci Rep. 2017;7(1):1–8.
25. Liu H, Wu J, Min JH, Kim YK. One-pot synthesis and characterization of bifunctional Au-Fe3O4 hybrid core-shell nanoparticles. J Alloys Compd. 2012;537:60–64.
26. Oliveira-Filho GB, Atoche-Medrano JJ, Aragón FFH, Mantilla Ochoa JC, Pacheco-Salazar DG, da Silva SW, et al. Core-shell Au/Fe3O4 nanocomposite synthesized by thermal decomposition method: structural, optical, and magnetic properties. Appl Surf Sci. 2021;563:150290.
27. Umut E, Pineider F, Arosio P, Sangregorio C, Corti M, Tabak F, et al. Magnetic, optical and relaxometric properties of organically coated gold-magnetite (Au-Fe3O4) hybrid nanoparticles for potential use in biomedical applications. J Magn Magn Mater. 2012;324(15):2373–2379.
28. Slama Y, Arcambal A, Septembre-Malaterre A, Morel AL, Pesnel S, Gasque P. Evaluation of core-shell Fe3O4@Au nanoparticles as radioenhancer in A549 cell lung cancer model. Heliyon. 2024;10(8):e29297.
29. Xu X, Wu J, Dai Z, Hu R, Xie Y, Wang L. Monte Carlo simulation of physical dose enhancement in core-shell magnetic gold nanoparticles with TOPAS. Front Oncol. 2022;12:1–12.
30. Orlando T, Capozzi A, Umut E, Bordonali L, Mariani M, Galinetto P, et al. Spin dynamics in hybrid iron oxide-gold nanostructures. J Phys Chem C. 2015;119(2):1224–1233.
31. Lin FH, Doong RA. Catalytic nanoreactors of Au@Fe3O4 yolk-shell nanostructures with various Au sizes for efficient nitroarene reduction. J Phys Chem C. 2017;121(14):7844–7853.
32. Shevchenko EV, Bodnarchuk MI, Kovalenko MV, Talapin DV, Smith RK, Aloni S, et al. Gold/iron oxide core/hollow-shell nanoparticles. Adv Mater. 2008;20(22):4323–4329.
33. Liu H, Wu J, Min JH, Kim YK. One-pot synthesis and characterization of bifunctional Au-Fe3O4 hybrid core-shell nanoparticles. J Alloys Compd. 2012;537:60–64.
34. Umut E, Pineider F, Arosio P, Sangregorio C, Corti M, Tabak F, et al. Magnetic, optical and relaxometric properties of organically coated gold-magnetite (Au-Fe3O4) hybrid nanoparticles for potential use in biomedical applications. J Magn Magn Mater. 2012;324(15):2373–2379.
35. Oliveira-Filho GB, Atoche-Medrano JJ, Aragón FFH, Mantilla Ochoa JC, Pacheco-Salazar DG, da Silva SW, et al. Core-shell Au/Fe3O4 nanocomposite synthesized by thermal decomposition method: structural, optical, and magnetic properties. Appl Surf Sci. 2021;563:150290.
36. León Félix L, Coaquira JAH, Martínez MAR, Goya GF, Mantilla J, Sousa MH, et al. Structural and magnetic properties of core-shell Au/Fe3O4 nanoparticles. Sci Rep. 2017;7(1):1–8.
37. Perl J, Shin J, Schümann J, Faddegon B, Paganetti H. TOPAS: an innovative proton Monte Carlo platform for research and clinical applications. Med Phys. 2012;39(11):6818–6837.
38. Faddegon B, Ramos-Méndez J, Schuemann J, McNamara A, Shin J, Perl J, et al. The TOPAS tool for particle simulation, a Monte Carlo simulation tool for physics, biology and clinical research. Phys Med. 2020;72:114–121.
39. Schuemann J, McNamara AL, Ramos-Méndez J, Perl J, Held KD, Paganetti H, et al. TOPAS-nBio: an extension to the TOPAS simulation toolkit for cellular and sub-cellular radiobiology. Radiat Res. 2018;191(2):125–138.
40. Van Delinder KW, Khan R, Gräfe JL. Radiobiological impact of gadolinium neutron capture from proton therapy and alternative neutron sources using TOPAS-nBio. Med Phys. 2021;48(7):4004–4016.
41. Seo SJ, Han SM, Cho JH, Hyodo K, Zaboronok A, You H, et al. Enhanced production of reactive oxygen species by gadolinium oxide nanoparticles under core-inner-shell excitation by proton or monochromatic X-ray irradiation: implication of the contribution from the interatomic de-excitation-mediated nanoradiator effect to dose enhancement. Radiat Environ Biophys. 2015;54(4):423–431.
42. Banoqitah E, Djouider F. Dose distribution and dose enhancement by using gadolinium nanoparticles implant in brain tumor in stereotactic brachytherapy. Radiat Phys Chem. 2016;127:68–71.
43. De Vera P, Abril I, Garcia-Molina R. Energy spectra of protons and generated secondary electrons around the Bragg peak in materials of interest in proton therapy. Radiat Res. 2018;190(3):282–297.
44. Newhauser WD, Zhang R. The physics of proton therapy. Phys Med Biol. 2015;60(8):R155–R209.
45. Avasthi A, Caro C, Pozo-Torres E, Pernia Leal M, García-Martín ML, Puente-Santiago AR, et al. Magnetic nanoparticles as MRI contrast agents. Top Curr Chem. 2021;378(3):1–43.
46. Wei H, Bruns OT, Kaul MG, Hansen EC, Barch M, Wiśniowska A, et al. Exceedingly small iron oxide nanoparticles as positive MRI contrast agents. Proc Natl Acad Sci U S A. 2017;114(9):2325–2330.
47. Johny J, van Halteren CER, Cakir FC, Zwiehoff S, Behrends C, Bäumer C, et al. Surface chemistry and specific surface area rule the efficiency of gold nanoparticle sensitizers in proton therapy. Chemistry. 2023;29(50):e202301260.
48. Peukert D, Kempson I, Douglass M, Bezak E. Gold nanoparticle enhanced proton therapy: a Monte Carlo simulation of the effects of proton energy, nanoparticle size, coating material, and coating thickness on dose and radiolysis yield. Med Phys. 2020;47(2):651–661.
49. Mansouri E, Mesbahi A, Hamishehkar H, Montazersaheb S, Hosseini V, Rajabpour S. The effect of nanoparticle coating on biological, chemical and biophysical parameters influencing radiosensitization in nanoparticle-aided radiation therapy. BMC Chem. 2023;17(1):1–14.